Available online at www.sciencedirect.com
SCIENCE DIRECT®
PERGAMON
International Journal of Heat and Mass Transfer 46 (2003) 4201–4213
International Journal of HEAT and MASS TRANSFER
www.elsevier.com/locate/ijhmt

Entrainment in high-velocity, high-temperature plasma jets. Part I: experimental results

J.R. Fincke, D.M. Crawford, S.C. Snyder, W.D. Swank, D.C. Haggard, R.L. Williamson *

Idaho National Engineering and Environment Laboratory, P.O. Box 1625, Idaho Falls, ID 83415-2211, USA

Received 5 June 2002; received in revised form 22 April 2003

Abstract

The development of a high-velocity, high-temperature argon plasma jet issuing into air has been investigated. In particular the entrainment of the surrounding air, its effect on the temperature and velocity profiles and the subsequent mixing and dissociation of oxygen has been examined in detail. The total concentration of oxygen and the velocity and temperature profiles in the jet were obtained from an enthalpy probe. High-resolution Thomson scattering provided an independent measure of plasma velocity and temperature, validating enthalpy probe measurements and providing non-intrusive measurements near the nozzle exit. The concentration of atomic oxygen was obtained from 2-photon laser induced fluorescence. Molecular oxygen concentration and temperature was obtained from coherent anti-Stokes Raman spectroscopy. It was found that both the incompleteness of mixing at the molecular scale and the rate of oxygen dissociation and recombination affects jet behavior.

Keywords: Thermal plasma; Plasma spray; Jets; Entrainment; Laser diagnostics

1. Introduction

The thermal spray process is widely used for the production of high performance coatings. In this process micron-sized (5–100 μm) particulates are injected into a high-temperature (≈12,000 K, 10–30% ionized fraction), high-velocity (>1000 m/s, Mach number $\geqslant 0.5$), low density ($\rho_{\text{jet}}/\rho_{\text{ambient}} \approx 0.03$) plasma jet. The particulates are subsequently melted and accelerated through interaction with the jet and impacted onto a substrate to form a coating. The process is most often performed in a normal laboratory environment with the plasma jet issuing into surrounding air. These jets thus represent an industrially important class of compressible, partially ionized flows that are characterized by large density differences with the surrounding environment. Because of the high-temperatures involved, the density differences persist for relatively long distances even though the jet is rapidly diluted by entrainment of the surrounding fluid [1]. Entrainment alters the chemical composition and quickly slows and cools the jet, creating an oxidizing atmosphere and altering the efficacy of particle melting and acceleration.

In Part I of this work we will experimentally examine, in some detail, the entrainment process and the resulting characteristics of the plasma jet. In Part II detailed comparisons of experimental results will be made to computational results. The assessment of model performance is through comparison of calculated flow field characteristics to detailed experimental measurements that are described here. Measurements of plasma velocity, temperature, and entrained air fraction were obtained using a high-resolution laser scattering technique and an enthalpy probe integrated with a mass spectrometer. Measurements of the concentration of atomic oxygen were obtained using 2-photon laser induced fluorescence (LIF). Coherent anti-Stokes Raman Spectroscopy (CARS) was used to determine the temperature

* Corresponding author. Tel.: +1-208-526-0576.
E-mail address: rlw@inel.gov (R.L. Williamson).

0017-9310/$ - see front matter
doi:10.1016/S0017-9310(03)00272-2

Nomenclature

A	area, m^2
C_p	specific heat, J/kg K
D	anode exit diameter, m, or mass diffusion coefficient, m^2/s
h	gas enthalpy, J/kg
I	intensity, W
k	thermal conductivity, w/m s K, or reaction rate in gm, mole, K
m	mass flow rate, kg/s
M	Mach number
n	number density, $\#/m^3$
P	pressure, Pa
Pr	Prandtl number, v/k
Q_{plas}	energy input to plasma, W
R	ideal gas constant, J/kg mole K
$\bar{R}e$	average Reynolds number $= \rho_e v_e D/\mu_e$
Sc	Schmidt number, v/D
T	temperature, K
V, v	velocity, m/s

Greek symbols

α	thermal diffusivity, m^2/s, or Thomson scattering parameter
$\chi^{(3)}$	third order non-linear susceptibility
δ	shear layer thickness, m
Δ	differential
γ	ratio of specific heats
μ	viscosity, kg/m s
v	kinematic viscosity, m^2/s
λ	turbulence scale or wavelength, m
θ	scattering angle
ρ	density, kg/m^3
τ	time scale, s
ω	frequency, 1/s

Subscripts

c	chemical reaction
cw	cooling water
D	mass diffusion, or dissociation
e	exit condition
g	gas
in	initial or inlet properties
0	Kolmogorov microscale or centerline value
t	total or stagnation
α	thermal diffusion
λ	Kolmogorov scale
∞	freestream

of the entrained molecular oxygen and to estimate the local molecular oxygen concentration.

2. Jet characteristics

All testing was conducted using a commercial direct current plasma torch. The Miller SG-100 plasma torch was operated at 900 A and 15.4 V, with a standard anode and cathode arrangement (Miller #165 and #129 respectively). The torch nozzle exit diameter was 8.0 mm. The argon flow rate was 35.4 slm. The measured thermal efficiency of the torch under these operating conditions was 70%, and the atmospheric pressure was 85.5 kPa. At these conditions the arc attachment is diffuse and there is little power ripple due to arc dynamics. The voltage (power) ripple due to the switching of the power supply was ±10%. The predominant frequency is 180 Hz although other harmonics to 1440 Hz are present.

A pulsed laser (Q-switched, frequency doubled, Nd:YAG) schlieren photograph of the argon plasma jet is shown in Fig. 1. The exposure time is approximately 10 ns, fast enough to freeze this flow field. The plasma light is suppressed (though not completely so) by a narrow bandpass filter and the use of a mechanical shutter that is synchronized with the laser pulse. Based on measurements of temperature and velocity (described later) the centerline Mach number at the torch exit is approximately 0.49 and the centerline density ratio is

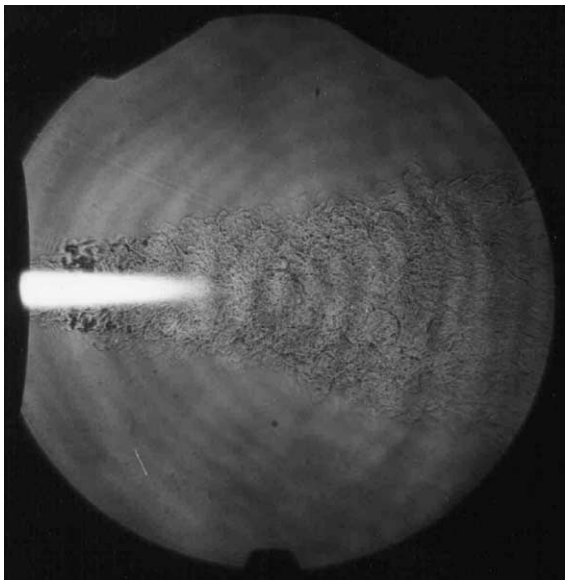

Fig. 1. Pulsed laser Schlieren of Ar plasma jet. For reference the image diameter is 75 mm.

$\rho_{jet}/\rho_{ambient} = 0.033$. The photograph indicates that the shear layer at the torch exit exhibits turbulence.

The jet Reynolds number, based on average plasma properties is $\bar{R}e = 615$, and is calculated as follows. The average exit enthalpy, h_e, is defined by $h_e = h_{in} + Q_{plas}/m$ where h_{in} is the initial enthalpy of the plasma gas, Q_{plas} is the energy input to the plasma, and m is the gas mass flow rate. The average exit velocity, v_e, is defined by $v_e = m/(\rho_e A)$ where A is the area of the anode exit and ρ_e is the average density at the exit. The average Reynolds number is then defined as $\bar{R}e = \rho_e v_e D/\mu_e$ where D is the diameter of the anode exit and μ_e is the plasma viscosity. The plasma properties of density and viscosity are uniquely determined by the exit pressure and average enthalpy, assuming thermodynamic equilibrium. For average Reynolds numbers greater than about 400 the shear layer is turbulent at the exit of the torch [2]. This is due to the cold, relatively high Reynolds number boundary layer on the anode wall undergoing transition inside the torch. Because of the high-temperature, low density, and relatively large viscosity in the center of the flow field, the core region at the exit remains substantially laminar.

A qualitative conceptual model, which describes the main features of the entrainment process, and estimates the important time scales, has been proposed by Broadwell and Briedenthal [3]. The model describes the entrainment and mixing process as a sequence of events initiated by the engulfment or induction of irrotational fluid into the jet shear layer. This initial process is kinematic and not diffusive with the irrotational fluid immediately adjacent to the shear layer participating in the large-scale structure motion of the shear layer long before it has acquired vorticity of its own. These entrained or inducted "lumps" of fluid are subsequently strained and broken down into smaller and smaller spatial scales or eddys. During this process the interfacial area rapidly increases until the viscous Kolmogorov microscale, λ_0, is reached. Once λ_0 is reached and the interfacial zones intermingle, molecular diffusion and heat conduction annihilate the local concentration and temperature gradients. For large Reynolds numbers a dimensional argument yields an expression for the time required for the cascade in time scales [3] to reach a given spatial scale, λ. The time to reach the Kolmogorov scale is $\tau_{\lambda_0} \approx k_1 \delta/1/2V_0$, where V_0 is the jet centerline velocity, δ is the thickness of the shear layer, and k_1 is a constant of order unity. The time to diffuse or equilibrate across an eddy of scale λ is $\tau_{\lambda_D} = \lambda^2/D$ for mass diffusion or $\tau_{\lambda_\alpha} = \lambda^2/\alpha$ for temperature equilibration where D is the mass diffusion coefficient and α is the thermal diffusivity. The Damkohler number is the ratio of the mixing or diffusion time scale to the chemical reaction time scale; τ_{λ_0}/τ_c for breakup of the large scales and τ_{λ_D}/τ_c and τ_{λ_k}/τ_c for diffusion across the small scales [4], where τ_c is the chemical reaction time constant. Large Damkohler numbers tend towards mixing limited chemistry while small values tend toward reaction rate limited chemistry.

An intermediate stage that may precede the final stage of gradient annihilation to a significant extent is also associated with the diffusive processes of molecular mixing and heat conduction. The corresponding diffusion scale λ_D differs from the Kolmogorov scale by the inverse of the square root of the Schmidt number [5], $\lambda_D = \lambda_0 S_c^{-1/2}$. Similarily for heat transfer by the inverse square of the Prandtl number, $\lambda_\alpha = \lambda_0 Pr^{-1/2}$. This intermediate stage, sometimes referred to as infusion, is indistinguishable in gases ($S_c \approx Pr \approx 1$) from the final diffusive dominated process occurring at the Kolmogorov scale. Because of the very large temperature gradients present in high-temperature jets, significant heat transfer at the boundaries of cold inducted eddies may occur before the fluid is mixed at the Kolmogorov scale making this intermediate stage process particularly significant. For the case of the dissociation of oxygen and nitrogen entrained in a high-temperature plasma jet this stage of the entrainment process may result in substantial amounts of entrained gas becoming dissociated for times significantly less than the time for complete equilibration of the smallest scales.

For high-temperature plasma jets density effects are also important. Increased mixing and entrainment in low density jets and mixing shear layers when the high speed fluid is at lower density has been previously observed by a number of authors [6–8]. Reducing the density ratio below 0.72 leads to jet instability [9,10] resulting in the formation of large unsteady axisymmetric vortex structures that rapidly increase fluid induction. The inherent unsteadiness of the jet is further influenced by discharge and power supply driven power fluctuations. These fluctuations result in the formation of large-scale perturbations that are on the order of the jet radius in size. While many studies of jet behavior exist, individual published results are difficult to compare directly because the nozzle exit, boundary-layer characteristics have a strong influence on jet development [11].

3. Enthalpy probe measurements

Originally developed in the 1960s, enthalpy probes [12] have been widely applied to thermal plasmas [13–17] and their performance in thermal plasma jets has been validated by direct comparison to laser scattering measurements [15,16]. The enthalpy probe is a water-jacketed gas sampling and stagnation pressure probe from which the enthalpy, temperature, and velocity of a hot flowing gas can be derived once the composition is known. The probe used in this study is copper with an outside diameter of 4.76 mm and a hemispherical tip.

Probe survivability in high-temperature and high-velocity flows dictates a large probe size. The gas composition is obtained from a differentially pumped quadrapole mass spectrometer [17]. For low Mach number flows the free stream velocity, v_∞, is obtained from $v_\infty = [2(P_t - P_\infty)/\rho_\infty]^2$ where P_t is the stagnation pressure, P_∞ is the ambient or static pressure, and the density ρ_∞ is a function of the freestream enthalpy, pressure and gas composition. At Mach numbers where compressibility effects are important the flow is assumed to stagnate isentropically with frozen composition [16]. The Mach number is then obtained from the measured pressure ratio $(P_\infty/P_t) = (1 + ((\gamma-1)/\gamma)M^2)^{-\gamma/\gamma-1}$ and the velocity is obtained from $v_\infty = M[\gamma R T_\infty]^{1/2}$ where T_∞ corresponds to the freestream enthalpy and pressure. The freestream enthalpy, h_∞, is the measured total enthalpy minus $0.5v^2$ and is obtained by iteration with the velocity calculation.

Centerline velocity, temperature, and entrained air data derived from enthaply probe measurements are shown in Figs. 2 and 3 and the corresponding calculated Mach number and density ratio are shown in Fig. 4. The axial coordinate is measured from the face of the torch and the lines are fits to the experimental data. Particularly noticeable is the rapid increase in air content and the associated slowing and cooling of the jet although the large density difference between the jet and surrounding fluid persist well downstream. The corresponding radial profiles of velocity, temperature and entrained air data are shown in Figs. 5–7. The jet is not perfectly symmetric due to the way in which the arc strikes and attaches to the anode. Note that the temperatures are dependent on the assumption of thermodynamic equilibrium and reflect the mass-weighted average enthalpy of the mixture sampled.

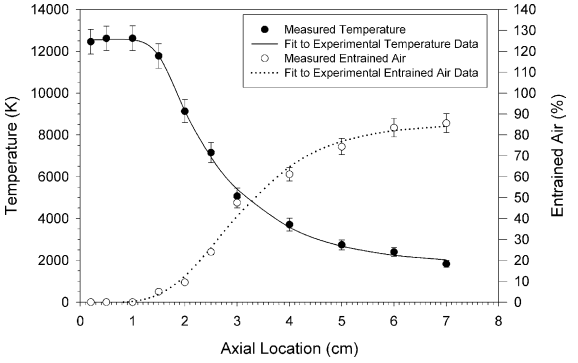

Fig. 3. Centerline temperature and entrained air fraction obtained from enthalpy probe measurements.

Because the gas sample is analyzed at more-or-less ambient conditions after cooling of the plasma gas, only stable species are observed. In analyzing enthalpy probe data to estimate plasma temperature, composition and density, a state of local thermodynamic equilibrium (LTE) is assumed corresponding to the measured enthalpy, composition and ambient pressure. More generally the measured composition, Figs. 3 and 7, is related to the plasma composition, without the assumption of thermodynamic equilibrium by the following:

$$\text{Air fraction} = \left.\frac{N_2 + O_2}{Ar + O_2 + N_2}\right|_{\text{ambient}} = \left.\frac{O_2 + \frac{1}{2}O + O_2^+ + \frac{1}{2}O^+ + N_2 + \frac{1}{2}N + N_2^+ + \frac{1}{2}N^+}{Ar + Ar^+ + O_2 + \frac{1}{2}O + O_2^+ + \frac{1}{2}O^+ + N_2 + \frac{1}{2}N + N_2^+ + \frac{1}{2}N^+}\right|_{\text{plasma}}$$

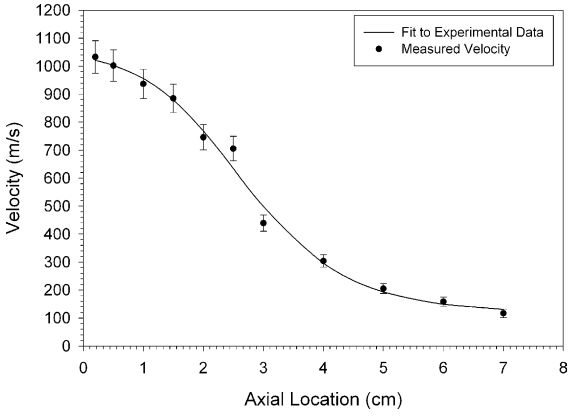

Fig. 2. Centerline velocity obtained from enthalpy probe measurements.

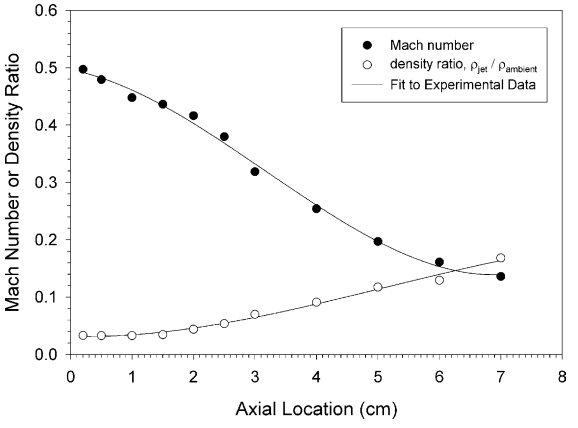

Fig. 4. Centerline Mach number and jet density ratio obtained from enthalpy probe measurements.

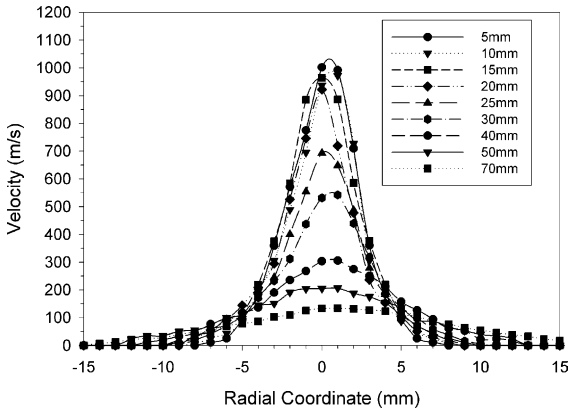

Fig. 5. Radial velocity profiles obtained from enthalpy probe measurements. Distances in the legend are axial locations measured form the face of the torch.

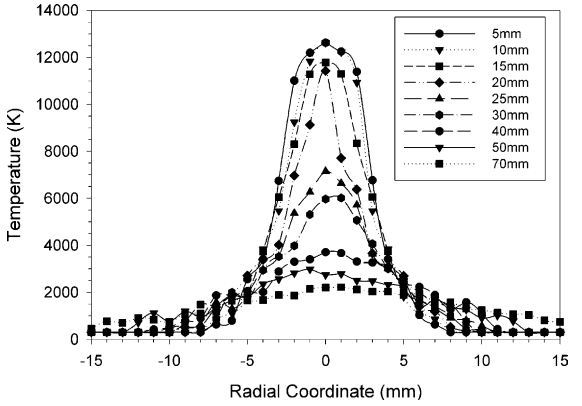

Fig. 6. Radial temperature profiles obtained from enthalpy probe measurements. Distances in the legend are axial locations measured form the face of the torch.

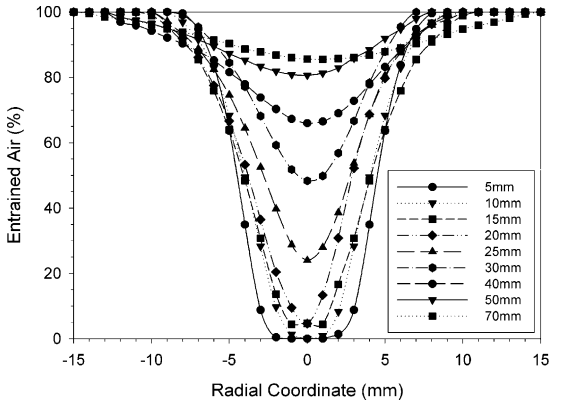

Fig. 7. Radial entrained air fraction profiles obtained from enthalpy probe measurements. Distances in the legend are axial locations measured form the face of the torch.

where the chemical symbol represents the mole density or number density of the species and NO_x species have been ignored. Similar expressions are derived for the argon fraction,

$$\left.\frac{\mathrm{Ar}}{\mathrm{Ar}+\mathrm{O_2}+\mathrm{N_2}}\right|_{\text{ambient}},\ \text{nitrogen fraction},$$

$$\left.\frac{\mathrm{N_2}}{\mathrm{Ar}+\mathrm{O_2}+\mathrm{N_2}}\right|_{\text{ambient}},\ \text{and oxygen fraction},$$

$$\left.\frac{\mathrm{O_2}}{\mathrm{Ar}+\mathrm{O_2}+\mathrm{N_2}}\right|_{\text{ambient}}.$$

4. Coherent Thomson scattering measurements

High-resolution lineshape analysis of elastically scattered laser light allows direct and non-intrusive measurement of the plasma velocity and gas or heavy particle temperature [15,16,18,19]. Interpretation of lineshape data does not depend on LTE assumptions or reliance on non-LTE models, although Maxwell–Boltzmann kinetic energy distributions are usually assumed for each species. In principle, the technique is applicable to multi-component mixtures, however interpretation is most reliable for single component plasmas. Results are therefore practically limited to the near nozzle region of the jet prior to the entrainment of substantial quantities of air. The plasma velocity is obtained by choosing a scattering geometry such that the difference between the scattered light wave vector and the incident laser wave vector has a component along the flow velocity. The lineshape will then be Doppler shifted relative to the incident laser frequency and the bulk gas velocity is determined.

For typical atmospheric pressure thermal plasmas, collective effects become important and scattering is referred to as coherent Thomson scattering. For this case the total lineshape consists of the central ion feature (with a width of 10–15 GHz), and well separated sharp electron feature resonance peaks, or plasma lines that are located in the ±3000–5000 GHz range. The ion feature also exhibits resonance structure due to scattering from ion-acoustic waves [20] evident in the two humps of the experimental ion feature spectrum of Fig. 8. The ion feature is dependent on but relatively insensitive to electron temperature and number density and is determined primarily by the heavy particle temperature.

High-resolution ion-feature lineshape measurements, shown schematically in Fig. 9, with a good signal-to-noise ratio (SNR) require the use of high peak power, narrow linewidth laser sources and high-resolution analysis of the scattered light. A pulsed, frequency-doubled, injection seeded Nd:YAG laser and a scanning, high finesse, Fabrey–Perot interferometer (F–PI) are used. The 10 ns duration laser/pulses have a nearly

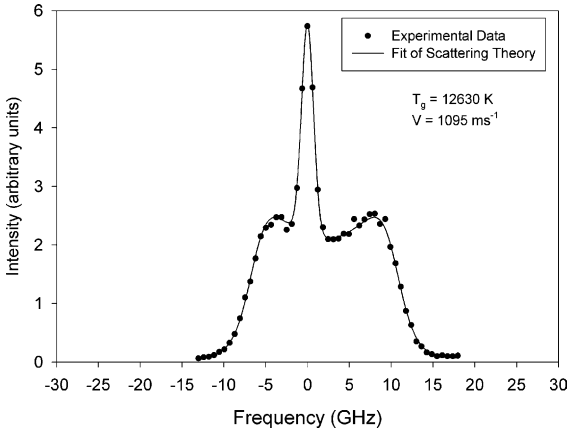

Fig. 8. Typical fully resolved ion-feature lineshape. The central spike is reference light from the laser source and the double humped ion feature is frequency shifted due to the bulk plasma velocity. The solid line is the fit of the theory to the experimental data yielding a temperature of 12,630 K ± 7% and a velocity of 1095 m/s ± 3%.

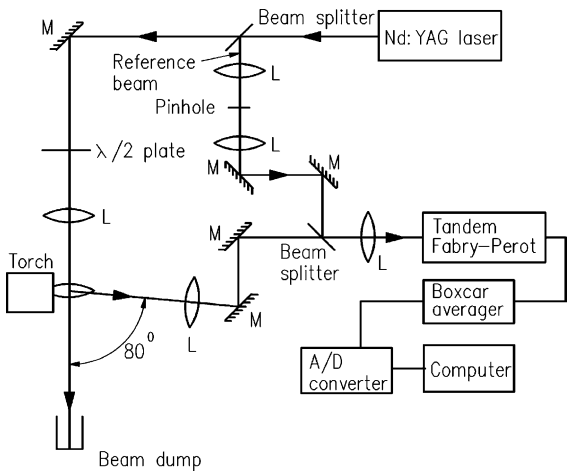

Fig. 9. Schematic of high-resolution Thomson scattering experiment.

transform limited bandwidth of ≈100 MHz. The scattering geometry is chosen such that the difference between the scattered and incident wave vectors has a component along the flow velocity of the plasma jet, Fig. 9, and the lineshape of the scattered light is Doppler shifted. A small amount of laser light is split off of the main beam, Fig. 9, and focused into the F–PI to act as a frequency reference from which Doppler shifts due to the gas velocity are measured. The central narrow peak in the lineshape in Fig. 8 is the F–PI response to the reference laser beam and the flow velocity is determined from the Doppler shift of the scattered light relative to the incident laser frequency. The output of the F–PI is detected with a photomultiplier tube and boxcar average synchronized to the firing of the laser. The recorded lineshape typically represents the average of 50 successive scans over a period of 250 s. The spatial resolution is approximately 3×10^{-3} mm^3.

The ion-feature shown in Fig. 8 was measured on the jet centerline 2 mm downstream of the exit of the torch. The curve represents the least squares fit of the data to the theory. The one-sigma uncertainties of the temperature and velocity results in the center of the jet (Fig. 8) are 7% and 3% respectively. The measured radial profiles of velocity and temperature at an axial location of 2 mm are shown in Figs. 10 and 11 and compared with the enthalpy probe results. The apparent small radial registration error is due to slight differences in the way in which the plasma arc "struck" for the separate enthalpy probe and laser scattering experiments. The broadening of the profiles is due to the intrusive nature of the enthalpy probe [16] and is a function of the radial ve-

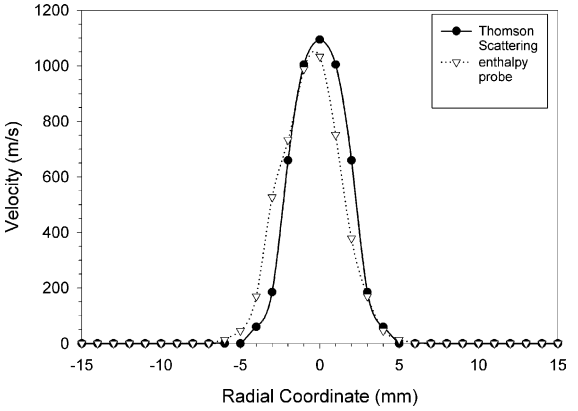

Fig. 10. Torch exit ($z = 2$ mm) radial velocity profiles measured by Thomson scattering and enthalpy probe techniques.

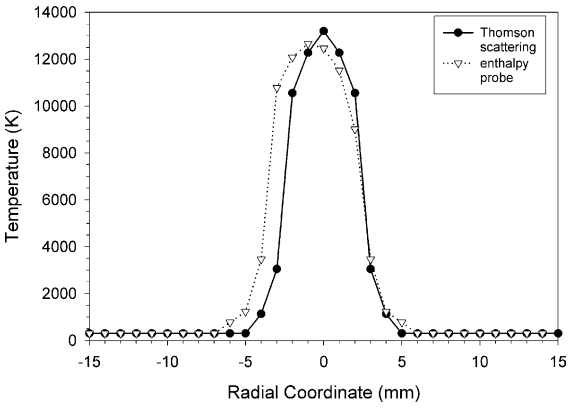

Fig. 11. Torch exit ($z = 2$ mm) radial temperature measured by Thomson scattering and enthalpy probe techniques.

locity gradient. That is, the stagnation or sampled streamline does not originate on the axis of the enthalpy probe. The streamline displacement is always towards the low velocity side of the jet; hence, the probe measures a streamline that originates in a higher-velocity, higher-temperature region. Because the streamline displacement is a function of the radial gradient, as the jet spreads and the gradient flattens the effect is significantly reduced. Hence the induced error is small except for the region near the torch exit where the radial gradients are the steepest. Thus, laser scattering is the preferred method of obtaining velocity and temperature profiles in regions where large radial gradients exist.

5. 2-Photon laser induced fluorescence measurements

Multiphoton excitation allows the creation, from the ground state, of observable populations of excited state O atoms [21–24]. A simplified energy level diagram for O is shown in Fig. 12. Two 225 nm photons excite the ground $2p^4\ ^3P$ state to the $3p\ ^3P$ state. The fluorescence signal at 844 nm results from the $3p\ ^3P$ to $3s\ ^3S$ transition. The laser used is a Nd:YAG pumped dye. The fundamental of the dye is doubled and mixed with the 1.06 μm fundamental from the YAG in a KDP crystal yielding 1 mJ of 225 nm light. The fluorescence signal was collected perpendicular to the laser beam and focused with 1:1 magnification onto the entrance slit (150 μm wide) of a 1 m focal length monochromator with an 1800 line/mm grating. The resulting measurement volume is on the order of 0.2 mm^3. The 2-photon LIF measurement is complicated by the extremely high quenching rates of the laser produced excited state. The observed lifetime of the 2-photon produced excited state ($3p\ ^3P$) under our conditions is less than 2 ns as compared to its natural undisturbed lifetime of 35 ns (Fig. 13).

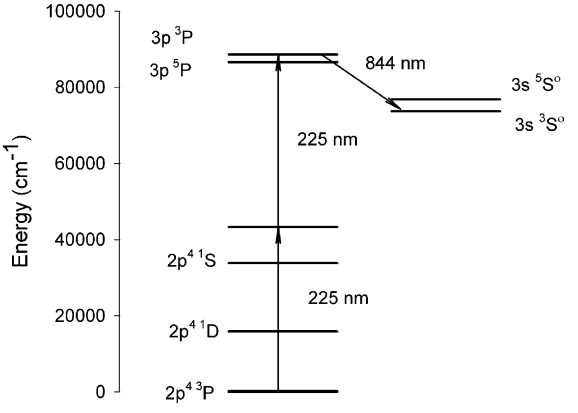

Fig. 12. Simplified atomic oxygen energy level diagram.

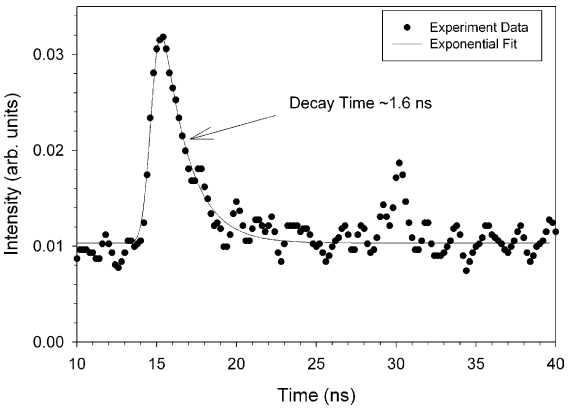

Fig. 13. Time resolved $2p^4\ ^3P$–$3p\ ^3P$ atomic oxygen fluorescence signal. The natural lifetime of the transition is 35 ns.

The measured centerline axial distribution of atomic oxygen obtained from 2-photon fluorescence is shown in Fig. 14. The measured decay time of the LIF signal is approximately constant (±20%) over the extent of the flow field, hence the intensity of the LIF signal is approximately proportional to the atomic oxygen concentration. Care is taken to perform measurements at power levels where the LIF intensity exhibits a quadratic dependence on laser intensity indicating that laser induced ionization does not influence excited state population densities. The measurement is calibrated against the enthalpy probe measurement of the total amount of oxygen observed ($O + 2O_2$) at an axial location of 20 mm where the temperature obtained from enthalpy probe measurements is high (≈6000 K). At this location it is assumed that entrained oxygen is completely dissociated. Examination of the data in Fig. 14 at axial locations of 15 and 25 mm indicates that the data and this assumption are self-consistent in that the estimated total oxygen concentration is essentially identical to the measured atomic oxygen concentration. This is also

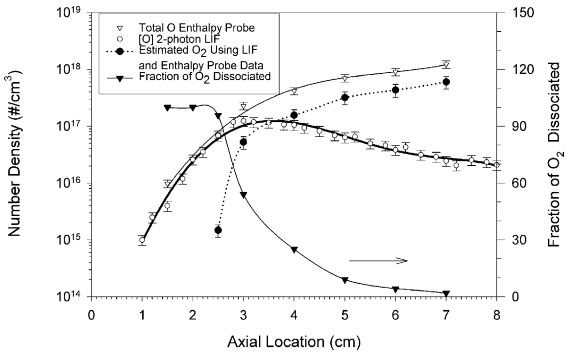

Fig. 14. Measured centerline distribution of atomic oxygen obtained from 2-photon fluorescence.

illustrated by the curve representing the fraction of O_2 that is dissociated plotted against the right hand ordinate. This assumption is further justified in the next section by the apparent absence of molecular oxygen observed in the CARS measurements at 15 and 25 mm. Also shown in Fig. 14 is the estimated concentration of molecular oxygen calculated from the difference of the enthalpy probe and LIF measurements. The total number density of oxygen atoms is estimated from the enthalpy probe data noting that:

$$\text{Total oxygen} = 2O_2 + O + 2O_2^+ + O^+ = 2\frac{O_2}{Ar + O_2 + N_2}\bigg|_{\text{ambient}}\left[n_t - \left(n_e + \tfrac{1}{2}O + \tfrac{1}{2}O^+ + \tfrac{1}{2}N + \tfrac{1}{2}N^+\right)\right]$$

where the total mixture number density, n_t, is obtained from the perfect gas law and the other quantities inside the interior bracket on the right hand side are estimated assuming thermodynamic equilibrium using the temperature and composition obtained from the enthalpy probe. The maximum correction to n_t represented by the quantities inside the interior brackets is −15% with a worst case uncertainty associated with the assumption of equilibrium in the ±5% range.

Shown in Fig. 15 are the measured concentrations of atomic and molecular oxygen along with the corresponding equilibrium concentrations derived from enthalpy probe measurement of temperature and total oxygen. In general the centerline dissociation of molecular oxygen slightly lags equilibrium in the hot regions of the jet and the recombination lags the cooling of the jet. Fig. 16 contains radial profiles at four axial locations of atomic oxygen (2-photon LIF) molecular oxygen (difference between enthalpy probe and LIF measurements) and equilibrium concentrations calculated from enthalpy probe measurements. In the jet near field (axial location = 10 and 20 mm) the dissociation of molecular oxygen is complete on the centerline of the jet (corresponding to the calibration constraint) but significantly lags the equilibrium concentration in the turbulent mixing layer. Further downstream (30 mm) the apparent degree of dissociation slightly lags the equilibrium value and again approaches equilibrium at 50 mm. In all cases the observed oxygen atom concentrations in the relatively cold fringes of the jet exceed the equilibrium values suggesting that the rate of turbulent diffusion is greater than the rate of recombination at these temperatures.

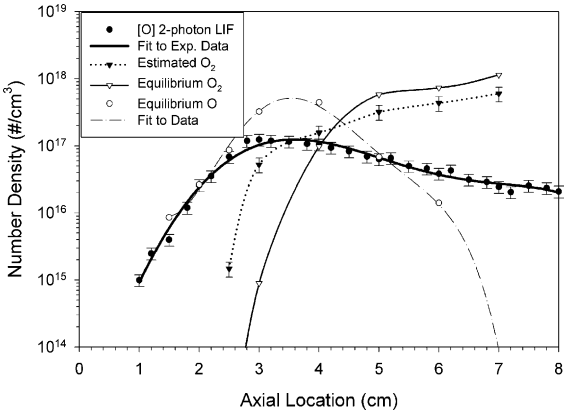

Fig. 15. Measured centerline distribution of atomic and molecular oxygen compared to equilibrium concentrations corresponding to enthalpy probe measurements.

6. Coherent anti-Stokes Raman spectroscopy measurements

The CARS technique [25–28] is applicable to the measurement of the temperature and concentration of any Raman active species present in sufficient quantities to yield a CARS signal. A CARS signal is generated when two laser beams at frequency ω_1, (termed the pump beams) and one laser beam at frequency ω_2 (termed the Stokes beam) interact through the third order non-linear susceptibility of the medium $\chi^{(3)}$. This interaction generates an oscillating polarization and thus coherent (laser like) radiation at frequency $\omega_3 = 2\omega_1 - \omega_2$. The spectral shape is determined by the frequency dependence of the susceptibility [28]. The third order susceptibility is a complex quantity and is composed of a resonant (χ_r) and a non-resonant (χ_n) component. Because our pump beam is transform limited in spectral bandwidth (≈100 MHz) the cross-coherence effects present when multi-mode YAG lasers are used can be neglected. Furthermore it is assumed that the CARS lines are superimposed without interaction (isolated line approximation) and are homogeneously broadened. For the case in which the non-resonant background is suppressed by choosing certain polarizations of the pump and Stokes beams (polarized CARS) (Fig. 17) then $I_3 \propto n^2|\bar{\chi}_r|^2 I_1^2 I_2$. The particle density, n, is obtained by absolute intensity measurement of the CARS signal. The temperature is determined from the relative vibrational and rotational populations or the spectral shape of the CARS signal.

A non-planar BOXCARS [28] beam configuration was used to maximize the spatial resolution of the system while satisfying the phase matching requirements for signal generation. This apparatus is shown schematically in Fig. 17. The focusing and recollimating lens focal lengths are 500 mm. The CARS sample volume is roughly defined by the overlap of the laser beams and is approximately 1.5–2 mm in length with an estimated diameter of 200 μm. Single shot data is acquired and

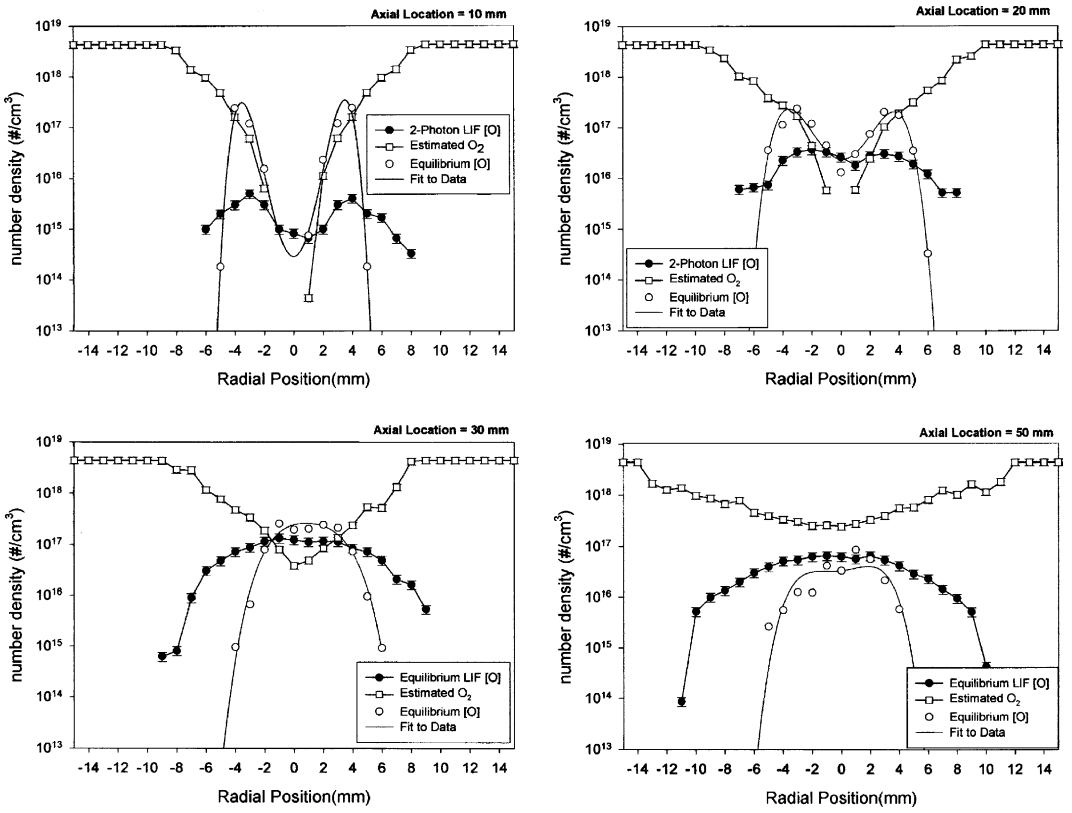

Fig. 16. Measured radial distributions of atomic oxygen, equilibrium concentration calculated from enthalpy probe measurements and estimated molecular oxygen concentrations.

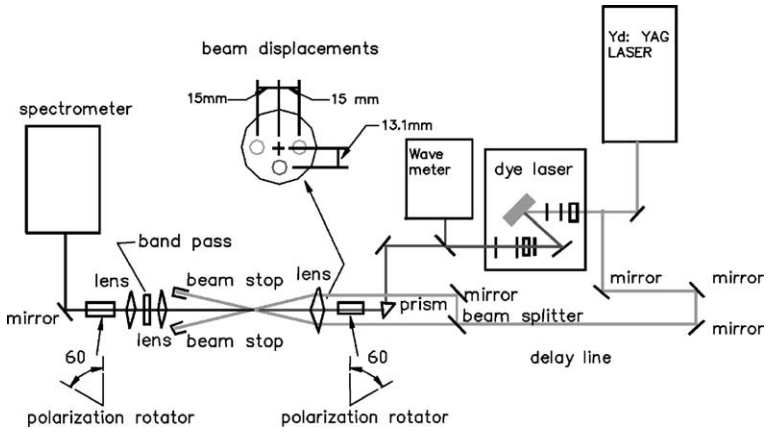

Fig. 17. Schematic of polarized CARS apparatus. There is a 120° angular rotation between the signal and probe beams.

stored by a gated, intensified diode array at the focal plane of a 1 m spectrometer.

A typical single shot Q-branch CARS oxygen spectra taken at 1100 K is shown in Fig. 18. Overlaid with the experimental data is a theoretical spectra calculated using a modified version of the CARSFT [29] computer code. The feature between 579.0 and 579.2 nm is the so called hot band, originating from the $v = 2$ to $v = 1$ rotational–vibrational transitions. The temperature is determined by least squares fit of the theoretical

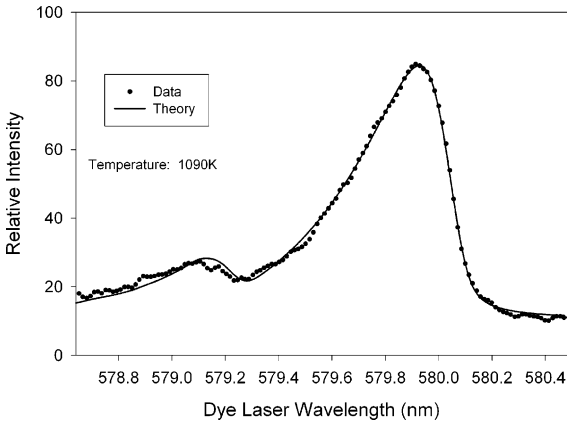

Fig. 18. Typical experimental CARS O_2 spectrum and theoretical lineshape fit.

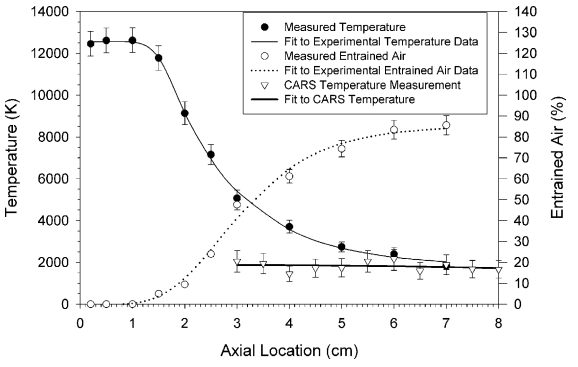

Fig. 19. Axial comparison of CARS O_2 temperature and enthalpy probe mixture temperature.

distribution to the data with temperature as a parameter. The species density measurement, which is dependent upon measurement of the absolute intensity of the CARS signal, is complicated by intensity fluctuations of the lasers and changes in beam overlap, while the temperature measurement is primarily dependent on relative measurements and is less affected. In non-isothermal flowfields CARS temperature measurements are also significantly effected by spatial averaging effects. The relevant length scales (limited by the Kolmogorov scale) cause both hot and cold gases to be simultaneously present in the CARS measurement volume. When temperature gradients occur the observed CARS signal is a spatial average of the component signals and the CARS temperature can be very different from the true (mass weighted) average [30–32]. Because of the number density squared dependence of CARS the result is heavily weighted toward the cold gas. Even small amounts of cold gas (1–10%) can dramatically lower the apparent temperature derived by fitting a CARS lineshape and must be taken into consideration when evaluating the data acquired in the intermittency region of an entraining flowfield.

Fig. 19 compares the rotational–vibrational temperature of molecular oxygen obtained from the CARS measurement to the temperature obtained from the enthalpy probe on the centerline of the jet. For locations closer to the torch face than 30 mm the concentration of molecular oxygen is insufficient ($<1\times10^{16}$ #/cm^3) to yield a CARS signal, hence the oxygen present (Figs. 3 and 14) is almost, if not, completely dissociated further validating the assumption of complete dissociation used in calibrating the LIF signal. As is evident in the plot the molecular oxygen rotational temperatures are significantly less than the mixture temperatures obtained from the enthalpy probe, indicating that measurable amounts of relatively cold air are rapidly inducted deep into the jet flow. These cold eddys are not yet fully mixed and equilibrated with the hot plasma gas. At 60 mm the mixing process is relatively complete and the two temperature measurements converge. While significant temperature differences exist at 30 mm, 6000 K average plasma temperature compared to 2500 K molecular oxygen temperature, 50% of the entrained oxygen is dissociated leaving 50% as "cold" molecular oxygen (Fig. 14). This suggests that the process of infusion occurring at the boundaries of small and intermediate size eddies driven by large gradients is producing significant quantities of dissociated oxygen. Little variation in the axial distribution of the CARS temperature is observed, presumably due to the strong weighting towards the colder gas.

The radial distribution of temperature derived from the enthalpy probe and CARS temperature measurements are shown in Fig. 20. In the jet fringes the CARS and enthalpy probe measurements converge. Within the mixing layer cold eddies are clearly present. In this layer the CARS signal exhibits shot-to-shot variation from a very strong signal corresponding to a "cold" CARS spectrum to a complete absence of signal indicating that the local molecular oxygen concentration is less than the detection limit of approximately 1×10^{16} #/cm^3. While we were able to obtain estimates of molecular oxygen concentration from the power normalized CARS signal (Fig. 21) and the estimates are reasonably (within a factor of 2 or so) matched to the value obtained form the differences of the enthalpy probe and 2-photon measurements in the mean, the shot-to-shot variation was not analyzed. This is due to the large shot-to-shot variation associated with beam alignment and beam steering present in the turbulent non-isothermal flow field, as well as uncorrelated pulse-to-pulse variations between the YAG and dye lasers. Hence, the CARS data should be interpreted as a clear indication of the induction and persistence of cold eddys in the jet but further quantitative interpretation of either temperature or concentration is probably unwarranted.

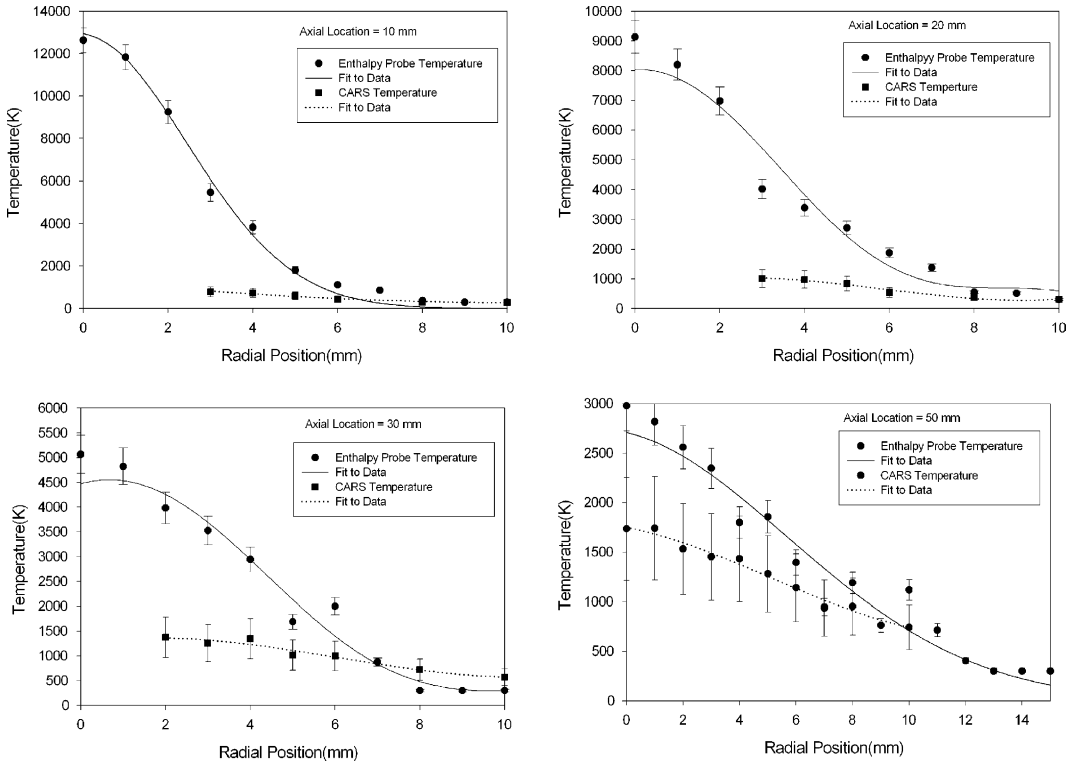

Fig. 20. Radial comparison of CARS O_2 temperature and enthalpy probe mixture temperature.

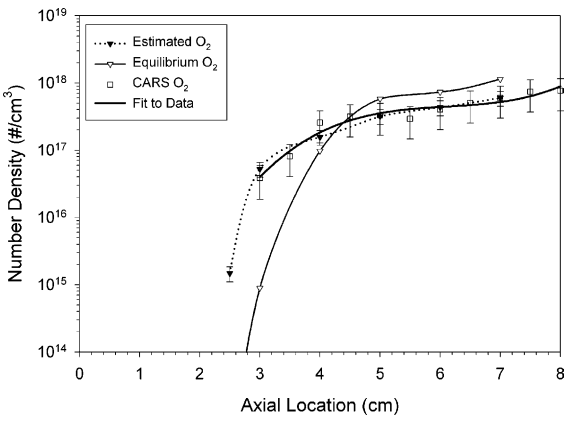

Fig. 21. Comparison between measured and calculated total and molecular oxygen concentrations.

7. Conclusions

The CARS temperature and concentration measurements clearly indicate the presence of "cold" molecular oxygen on the centerline of the jet beginning at an axial location of 30 mm which persists well downstream in the jet, finally equilibrating at 60–70 mm (Fig. 19). The scale of the smallest (Kolmogorov scale) eddies at 30 mm is estimated [33] to be on the order of 0.1 mm using $\lambda_0 = \delta Re^{-3/4}$ where the centerline values of temperature and velocity and the half-width of the jet were used in calculating the Reynolds' number. This scale is somewhat smaller than the apparent small eddy size of 0.5 mm or so suggested by the Schlieren photograph. The time to mix to the Kolmogorov scale is on the order of $\tau_\lambda = \delta/\Delta v = 0.01/250 = 40$ μs. The time for temperature equilibration $\tau_k = \lambda^2/\alpha$ is on the order of 50 μs where the properties of air at 1000 K were used for the thermal diffusivity. Hence the time to reach the smallest scales and the time required for equilibration are of the same order of magnitude. Thus cold ambient air that is continually convected into the jet and carried downstream can survive for tens of millimeter during the eddy breakup and equilibration process.

The dissociation reaction for oxygen is $O_2 + M \longleftrightarrow O + O + M$ where $M = Ar, O_2, N_2, e^-, \ldots$ In the jet near field the time constant for this reaction is approximately $\tau_d = 1/(2[M]k_D)$ where the reaction rate is $k_D = 20 \times 10^{21} T^{-1.5} \exp(-59{,}500/T)$ in terms of gm mole K [34]. The estimated time constant for dissociation τ_d is on the order of 5 μs at 6000 K (the centerline temperature measured at ≈25 mm), which is relatively short compared to the time required for eddy break up and temperature equilibration. The corresponding Damkohler number is $\tau_{\lambda_k}/\tau_d = 10$. Thus the observation

of relatively cold, undissociated gas observed in the temperature data of Figs. 19 and 20 is consistent with the incompleteness of mixing. The fact that the apparent relative concentration of oxygen on the centerline between 1 and 3 cm is significant (Fig. 14) while little or no molecular oxygen is observed is apparently due to the process of infusion. In this region the high plasma jet temperature, 6000–12,000 K, results in substantial amounts of entrained gas becoming dissociated for times significantly less than the time for equilibration of the smallest scales.

The recombination process (the reverse dissociation reaction) takes place at a relatively low temperature, on the order of 2000 K. At this temperature the time constant for recombination is on the order of $\tau_r = 1$ ms suggesting a greater influence of the rate of reaction. On both the centerline ($z > 5$ cm) (Fig. 15) and in the jet fringes (Fig. 16) the concentration of atomic oxygen exceeds equilibrium values. One should note that while cold eddys can survive for extended periods of time, hot eddys have a shorter characteristic equilibration time, $\tau_{\lambda_k} \approx 10$ μs, resulting in a Damkoler number of $\tau_{\lambda_k}/\tau_r \approx 0.01$ suggesting the importance of the rate of recombination. The data indicate that significant departures from equilibrium are present in the rapidly entraining, high-temperature plasma jet studied and that mixing to the molecular level is incomplete over a substantial portion of the flowfield. The incompletness of mixing contributes to the apparent departures from equilibrium as does the rate of recombination as the jet spreads and cools.

Acknowledgements

This work was supported by the US Department of Energy, Office of Energy Research, Office of Basic Energy Sciences, Division of Engineering and Geosciences, Engineering Research under DOE Idaho Field Office Contract DE-AC07-99ID13727.

References

[1] E. Pfender, J.R. Fincke, R. Spores, Entrainment of cold gas into thermal plasma jets, Plasma Chem. Plasma Process 11 (1991) 529–543.
[2] J.R. Fincke, G.C. Pentecost, Laminar to turbulent transition and entrainment in thermal plasma jets, in: Proceedings of the 28th National Heat Transfer Conference, Heat Transfer in Thermal Plasma Processing, HTD-Vol. 161, American Society of Mechanical Engineers, 1991, p. 101–106.
[3] J.E. Broadwell, R.E. Breidenthal, A simple model of mixing and chemical reaction in a turbulent shear layer, J. Fluid Mech. 125 (1982) 397–410.
[4] M.G. Mungal, P.E. Dimotakis, Mixing and combustion with low heat release in a turbulent shear layer, J. Fluid Mech. 148 (1984) 349–382.
[5] P.E. Dimotakis, Two-dimensional shear-layer entrainment, AIAA J. 24 (1986) 1791–1796.
[6] G.L. Brown, A. Roshko, On density effects and large structure in turbulent mixing layers, J. Fluid Mech. 64 (1974) 775–816.
[7] F.P. Ricou, D.B. Spalding, Measurements of entrainment by axisymmetrical turbulent jets, J. Fluid Mech. 11 (1961) 21.
[8] B.N. Abramovich, O.V. Yakovlevsky, I.P. Smirnova, A.N. Secundov, S.Y. Krashensnnikov, An investigation of the turbulent jets of different gases in a general stream, Astronaut. Acta 14 (1969) 229.
[9] P.A. Monkewitz, K.D. Sohn, Absolute instability in hot jets, AIAA J. 26 (1988) 911–916.
[10] S. Russ, P.J. Strykowski, Turbulent structure and entrainment in heated jets: The effect of initial conditions, Phys. Fluids A 5 (1993) 3216–3225.
[11] J. Lepicovsky, Total temperature effects on centerline Mach number characteristics of freejets, AIAA J. 28 (1990) 478–482.
[12] J. Grey, P.F. Jacobs, M.P. Sherman, Calorimetric probe for the measurement of extremely high temperatures, Rev. Sci. Instr. 33 (1962) 738–741.
[13] M. Brossa, E. Pfender, Probe measurements in thermal plasma jets, Plasma Chem. Plasma Process 8 (1988) 75–90.
[14] A. Capetti, E. Pfender, Probe measurements in argon plasma jets operated in ambient argon, Plasma Chem. Plasma Process 9 (1989) 329–341.
[15] J.R. Fincke, S.C. Snyder, W.D. Swank, D.C. Haggard, Comparison of enthalpy probe and laser light scattering measurement of thermal plasma temperatures and velocities, Rev. Sci. Instr. 64 (1993) 711–724.
[16] J.R. Fincke, S.C. Snyder, W.D. Swank, D.C. Haggard, Enthalpy probe performance in compressible thermal plasma jets, Rev. Sci. Instr. 64 (1994) 3585–3593.
[17] W.D. Swank, J.R. Fincke, D.C. Haggard, Modular enthalpy probe and gas analyzer for thermal plasma measurements, Rev. Sci. Instr. 64 (1993) 56–62.
[18] S.C. Snyder, L.D. Reynolds, G.D. Lassahn, J.R. Fincke, C.B. Shaw, R. Kearney, Determination of gas temperature and velocity profiles in an argon thermal plasma jet by laser light scattering, Phys. Rev. E 47 (1993) 1996–2005.
[19] H.J. Kunze, The laser as a tool for plasma diagnostics, in: W. Lochte-Holtgreven (Ed.), Plasma Diagnostics, American Elsevier Publishing Co., Inc, New York, 1968.
[20] T.P. Hughes, Plasmas and Laser Light, John Wiley and Sons, New York, 1975.
[21] W.K. Bischel, B.E. Perry, D.R. Crosley, Detection of fluorescence from O and N atoms induced by two-photon absorption, Appl. Opt. 21 (1982) 1419–1429.
[22] W.K. Bischel, B.E. Perry, D.R. Crosley, Two-photon laser-induced fluorescence in oxygen and nitrogen atoms, Chem. Phys. Lett. 82 (1982) 85–88.
[23] M. Alden, U. Westblom, J.E.M. Goldsmith, Two-photon-excited stimulated emission from atomic oxygen in flames and cold gases, Opt. Lett. 14 (1989) 305–307.
[24] L.F. DiMauro, R.S. Gottscho, T.A. Miller, Two-photon laser-induced fluorescence monitoring of O atoms in a

plasma etching environment, J. Appl. Phys. 56 (1984) 2007–2011.
[25] R.R. Antcliff, O. Jarrett, Multispecies coherent anti-Stokes Raman scattering instrument for turbulent combustion, Rev. Sci. Instr. 58 (1987) 2075–2080.
[26] A.C. Eckbreth, G.M. Dobbs, J.H. Stufflebeam, P.A. Tellex, CARS temperature and species measurements in augmented jet engine exhausts, Appl. Opt. 23 (1984) 1328–1339.
[27] L.P. Gross, D.D. Trump, B.G. MacDonald, G.L. Switzer, 10-Hz coherent anti-Stokes Raman spectroscopy apparatus for turbulent combustion studies, Rev. Sci. Instr. 54 (1983) 563–571.
[28] M.D. Levenson, Introduction to Nonlinear Laser Spectroscopy, Academic Press, New York, 1982.
[29] R.E. Palmer, The CARSFT computer code for calculating coherent anti-Stokes Raman Spectra: user and programmer information, SAND89-8206, Sandia National Laboratory Report, 1989.
[30] J.D. Garman, D. Dunn-Rankin, Spatial averaging effects in CARS thermometry of a nonpremixed flame, Combust. Flame 115 (1998) 481–486.
[31] T. Parameswaran, D.R. Snelling, Estimation of spatial averaging of temperatures from coherent anti-Stokes Raman spectroscopy, Appl. Opt. 35 (1996) 5461–5464.
[32] T. Parameswaran, D.R. Snelling, Effect of spatial averaging on CARS-derived temperatures, Combust. Flame 106 (1996) 511–514.
[33] P.E. Dimotakis, The mixing transition in turbulent flows, J. Fluid Mech. 409 (2000) 69–98.
[34] J.H. Park, E. Pfender, C.H. Chang, Reduction of chemical reactions in nitrogen and nitrogen–hydrogen plasma jets flowing into atmospheric air, Plasma Chem. Plasma Process 20 (2000) 165–181.